Environmental Science & Technology

pubs.acs.org/est

Article

Oxyanion Surface Complexes Control the Kinetics and Pathway of Ferrihydrite Transformation to Goethite and Hematite

Alireza Namayandeh,* Olaf J. Borkiewicz, Nefeli M. Bompoti, Maria Chrysochoou, and F. Marc Michel

Cite This: *Environ. Sci. Technol.* 2022, 56, 15672−15684

Read Online

ACCESS | Metrics & More | Article Recommendations | Supporting Information

ABSTRACT: The rate and pathway of ferrihydrite (Fh) transformation at oxic conditions to more stable products is controlled largely by temperature, pH, and the presence of other ions in the system such as nitrate (NO_3^-), sulfate (SO_4^{2-}), and arsenate (AsO_4^{3-}). Although the mechanism of Fh transformation and oxyanion complexation have been separately studied, the effect of surface complex type and strength on the rate and pathway remains only partly understood. We have developed a kinetic model that describes the effects of surface complex type and strength on Fh transformation to goethite (Gt) and hematite (Hm). Two sets of oxyanion-adsorbed Fh samples were prepared, nonbuffered and buffered, aged at 70 ± 1.5 °C, and then characterized using synchrotron X-ray scattering methods and wet chemical analysis. Kinetic modeling showed a significant decrease in the rate of Fh transformation for oxyanion surface complexes dominated by strong inner-sphere (SO_4^{2-} and AsO_4^{3-}) versus weak outer-sphere (NO_3^-) bonding and the control. The results also showed that the Fh transformation pathway is influenced by the type of surface complex such that with increasing strength of bonding, a smaller fraction of Gt forms compared with Hm. These findings are important for understanding and predicting the role of Fh in controlling the transport and fate of metal and metalloid oxyanions in natural and applied systems.

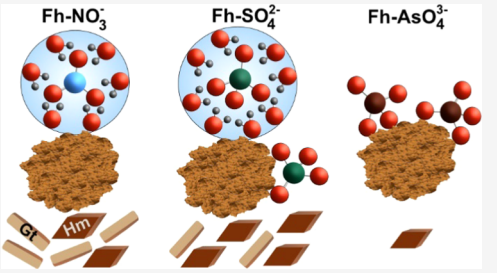

KEYWORDS: *ferrihydrite, oxyanion, transformation, arsenate, sulfate, nitrate, oriented attachment, dissolution/recrystallization*

INTRODUCTION

Nanosized iron oxides and hydroxides are abundant and important in the geochemical cycling of nutrients and contaminants. At acidic to intermediate pH, their surfaces are positively charged and have a particular affinity for metal and metalloid oxyanions such as nitrate (NO_3^-), sulfate (SO_4^{2-}), and arsenate (AsO_4^{3-}). These oxyanions associate with the mineral primarily through surface adsorption,[1−6] which immobilizes the ions, thereby affecting their transport and fate. However, adsorbed surface species can be remobilized during mineral transformations, which are common for iron oxides and hydroxides in (bio)geochemical systems. For example, under oxic conditions, ferrihydrite (Fh; $Fe_{1.0}O_{0.67}(OH)_{1.63}$),[7] a metastable iron oxy-hydroxide nanoparticle, eventually transforms to less hydrated and more stable goethite (Gt; α-FeOOH) and hematite (Hm; α-Fe_2O_3).[8−19] Surface area decreases during transformation due to crystal growth,[13] and changes in surface structure and reactivity impact the type and availability of surface functional groups. Combined, these changes generally reduce the capacity of the mineral surfaces for adsorption resulting in the release of oxyanions to solution.[11,13,20]

The transformation of Fh under oxic conditions involves a concurrent set of pathways forming Gt or Hm.[8,21] One pathway, dissolution/recrystallization, involves two steps: (1) a transition state achieved by dissolving Fh and (2) rapid Fe polymerization and precipitation of a solid (nano)crystalline product.[9,22,23] This process follows Ostwald's step rule.[24,25] Another pathway involves the aggregation, dehydration, and structural reorganization of Fh.[9,19,21,25−27] This pathway may include oriented attachment (OA) or nearly OA of precursors as part of the transformation and crystallization.[17] These pathways are not necessarily mutually exclusive, although one may be favored depending upon environmental conditions.

Experimental conditions are important in controlling synthetic Fh transformation in water.[27,28] The rate and pathway of synthetic Fh transformation in water are significantly controlled by pH,[8−12,17] although there is disagreement in the literature. For example, some studies show that low and high pHs promote the formation of Gt, whereas neutral pH favors Hm.[8,9,18,19] Others have reported Hm as the primary product at all pH conditions (2−10) across a varied range of temperatures (50−100 °C).[10] Many studies have examined the impacts of additional factors such as temperature[9,10] as well as structural impurities,[29,30] redox conditions in solution,[31−34] and the presence of certain organic ligands[35] and other ions,[11,13,14,16−18,35,36] especially metalloid

Received: July 10, 2022
Revised: September 16, 2022
Accepted: September 28, 2022
Published: October 11, 2022

https://doi.org/10.1021/acs.est.2c04971
Environ. Sci. Technol. 2022, 56, 15672−15684

oxyanions. For example, AsO_4^{3-}[11] and dissolved lead (as $Pb(NO_3)_3$)[14] were reported to slow the rate of Fh transformation, whereas NO_3^- and SO_4^{2-} promoted Hm and Gt formation at acidic conditions.[18] These studies have generally suggested that surface species control the rate and pathway of transformation. However, surface binding varies for different oxyanion species from weak electrostatic outer sphere to strong covalent inner sphere,[4,37−55] and the effects of oxyanion binding type/strength on the Fh transformation remain only partly understood.

Two different kinetic models have been used to describe the rate of Fh transformation. First-order kinetic models have mainly been used to evaluate the impacts of temperature and solution chemistry.[10,19,56] More recently, a second-order reaction equation was developed for the aggregation by OA of Gt during the Fh transformation.[17,57−59] We note that the models used in these studies rely only on the change in Fh concentration with time and do not account for the concurrent formation of Gt and/or Hm. A more comprehensive kinetic model should also include the rates of Gt and Hm formation.

The present study examines the effects of adsorbed NO_3^-, SO_4^{2-}, and AsO_4^{3-} on the rate and pathway of synthetic Fh transformation to Gt and Hm. The objective is to understand the impacts of oxyanion binding strength and type (i.e., strong inner sphere vs weak outer sphere) and pH (buffered vs nonbuffered). A new phase quantification method and kinetic model were developed to describe the effect of surface complexation type and strength on both the rates of Fh transformation and formation of Gt and Hm. The results are important for understanding the interactions between Fh and oxyanions in aqueous environments and their impacts on geochemical cycling.

MATERIALS AND METHODS

Ferrihydrite Synthesis and Batch Adsorption. Two-line Fh was synthesized using a modified version of Schwertmann and Cornell.[21] In brief, 0.2 M $Fe(NO_3)_3$ (ACS grade, Fisher Scientific) solution was prepared and titrated to pH 7.5 ± 0.2 using 1 M NaOH in less than 25 min. The resulting suspension was centrifuged and then dialyzed in several consecutive ultrapure (18.2 MΩ) water baths until the conductivity of the water dropped below 20 $\mu S\ cm^{-1}$. The resulting 5.0 g L^{-1} Fh suspension was transferred to 50 mL centrifuge tubes to prepare the batch samples needed for each experiment. For the SO_4^{2-} (FhS) and AsO_4^{3-} (FhAs) adsorption experiments, 5.0 mM Na_2SO_4 and 5.0 mM Na_2HAsO_4 (0.1 molar ratio SO_4^{2-} and AsO_4^{3-}/Fh) in a background of ∼100.0 mM $NaNO_3$ were added to the tubes, respectively, such that I was adjusted at 0.1 M. Two other sets of samples were prepared: one with 100.0 mM $NaNO_3$ (FhN) and one only including Fh to be used as a control. The pH of all of the samples was adjusted to 5.5 ± 0.2 using 1.0 M NaOH and HNO_3, and then they were shaken for 24 h to allow the adsorption process to reach equilibrium.[37,60,61]

The samples were centrifuged at 3500 rpm for 10 min and then filtered through a 0.22 μm filter. The solids were recovered, and supernatants were collected and analyzed using high-performance liquid chromatography-ion conductivity (IC) (SO_4^{2-} and NO_3^-) and inductively coupled plasma-optical emission spectroscopy (ICP-OES) (As) to determine the mass balance for the amount of oxyanion adsorbed on the Fh surface in each respective experiment.

All synthesis and transformation experiments were conducted in an air-equilibrated solution. MINTEQ was used to calculate the amount of dissolved inorganic carbon (DIC) in the solution, and surface complexation modeling was performed to measure the amount of DIC adsorbed on the Fh surface in the absence and presence of oxyanions. The details for the surface complexation modeling method are provided in Text S1.

Characterization of Oxyanion Surface Complexes. Based on the above protocol, the same set of samples was prepared to determine the coordination environments of the oxyanions using differential pair distribution function (d-PDF) analysis and *in situ* attenuated total reflectance Fourier transform infrared spectroscopy (ATR-FTIR). The adsorption experiment was conducted at pH 5.5 ± 0.2 for FhAs (d-PDF) and at pH 5.5 ± 0.2, 4.3 ± 0.2, and 3.0 ± 0.2 for FhS (d-PDF and ATR-FTIR) and FhN (ATR-FTIR). Synchrotron high-energy X-ray scattering measurements were conducted at beamline 11-ID-B at the Advanced Photon Source, Argonne National Laboratory. Samples were analyzed as wet suspensions loaded in 3 mm OD NMR Tubes. The raw scattering data were processed with GSAS-II. Using the xPDF suite,[62] the background was subtracted and reciprocal data converted to real-space PDFs using 24−25 $Å^{-1}$ as the max Q-space for the Fourier transform. The d-PDF was generated by subtracting the control PDF (FhN) from the PDFs of FhS and FhAs using Microsoft Excel. The scaling factor was optimized to remove the contribution of the Fe−O peak at ∼2 Å from the samples.

In situ ATR-FTIR experiments were conducted using a Bruker α II Fourier transform infrared (FTIR) spectrometer equipped with a platinum diamond-attenuated total reflection (ATR) sampling module and an OPUS 8 operating software suite. Briefly, a 25 μL of 5 g L^{-1} Fh suspension was deposited on the ATR diamond and dried under a nitrogen gas stream to create the Fh film. For SO_4^{2-} adsorption experiments, a peristaltic pump was used to inject 100 mM $NaNO_3^-$ on the Fh surface and acquire the background spectra. A 0.1 mM SO_4^{2-} solution in a background of 100 mM $NaNO_3$ was then flowed over the Fh film. Spectral data were collected for pH 5.5 ± 0.2, 4.3 ± 0.2, and 3.0 ± 0.2. The pH was adjusted using HNO_3.

For the NO_3^- adsorption experiment, the wet Fh suspension was taken as the background and then dried using nitrogen gas. The spectral data were collected by injecting 100 mM $NaNO_3^-$ on the Fh surface and incrementally adjusting the pH from 5.5 ± 0.2 to 3.0 ± 0.2 with HNO_3. All spectra were obtained by collecting 400 scans at 4 cm^{-1} resolution for a range of wavenumbers between 4000 and 400 cm^{-1}. IR spectra were continuously collected until there was no observable difference between the spectra, which indicated equilibrium and surface saturation.

Transformation Experiment and Sample Treatment. Two sets of samples were prepared for the transformation experiment, buffered and nonbuffered. For the buffered set, the wet pastes from the adsorption experiment were buffered at pH 5.5 ± 0.2 using 0.4 M 2-(*N*-morpholino)ethanesulfonic acid (MES) ($C_6H_{13}NO_4S$) and 2.0 M NaOH and transferred to a 10 mL high-density polyethylene (HDPE) plastic leak-proof opaque bottle. Three replicates were prepared for each time interval. The samples were placed in a sealed water bath and then heated at 70 ± 1.5 °C for up to 1200 h in a mechanical convection laboratory oven (Thermo Scientific Heratherm). This temperature was chosen because it results in

https://doi.org/10.1021/acs.est.2c04971
Environ. Sci. Technol. 2022, 56, 15672−15684

the formation of both Gt and Hm in the absence of oxyanions, which allowed us to study the impacts of outer-sphere and/or inner-sphere surface complexes on the transformation of Fh to these phases at reasonable laboratory timescales.[10] The sample preparation for the nonbuffered experiment was the same except that a known amount of deionized (DI) water was added in place of MES to keep the water/solid ratio the same in both sets of experiments. Samples were aged in the oven for different time points (0, 24, 48, 72, 120, 168, 240, 360, 600, 888, 1200 h). Removed samples were immediately transferred to a room-temperature water bath to cool. The pH of the samples was recorded, and then they were centrifuged at 3500 rpm for 10 min. The recovered pastes were air-dried under the hood for 24 h and ground to fine powders using mortar and pestle.

Liquid- and Solid-Phase Characterization. The aged samples were centrifuged at 3500 rpm for 10 min and then filtered through a 0.22 μm filter to separate oxyanions from corresponding solid particles. The same samples were ultracentrifuged (3K pore size) to collect the dissolved Fe in each sample. The supernatants were then analyzed by IC (NO_3^- and SO_4^{-2}) and inductively coupled plasma mass spectrometry (ICP-MS) (As and Fe) to measure the concentration of dissolved Fe and the oxyanions. Solids were analyzed as dry powders loaded in 1 mm OD polyimide capillaries using synchrotron high-energy X-ray scattering to identify and quantify the Fh and its transformation products. The raw scattering data were processed and converted to PDFs as described above.

Linear combination fitting (LCF, WinXAS[63]) of the PDFs was used to quantify phase abundances in the samples. Reference PDFs for synthetic 2-line Fh, Gt, and Hm were used to determine the concentrations of these phases in each sample. Fitting was performed from 0 to 20 Å, and the sum of the final concentrations was normalized to one. The reference PDFs were allowed minor shifts in r-space to account for differences in crystallinity between the references and samples. The LCF abundances were then used to calculate the rate of transformation. The transformation reactions, along with the rate law derivation, are provided in Texts S2 and S3 and discussed further in the next sections.

RESULTS AND DISCUSSION

Oxyanion Surface Complexes. The type of inner-sphere AsO_4^- and SO_4^{2-} surface complexes on Fh were examined using d-PDF. The d-PDF method is generally not sensitive to the presence of outer-sphere complexes.[38] In the case of AsO_4^{3-}, correlations observed at 1.71 and 3.29 $Å^{-1}$ correspond with As−O and As···Fe pairs, respectively (Figure S1), confirming the presence of bidentate binuclear inner-sphere complexes. This agrees with the previous d-PDF,[38] ATR-FTIR,[64] extended X-ray absorption fine structure (EXAFS),[65,66] and computational modeling[37,66−68] studies showing that inner-sphere complexation is the dominant mechanism of AsO_4^{3-} adsorption on Fh at intermediate to acidic pH. In the case of SO_4^{2-}, regardless of pH, the d-PDFs had two major peaks around 1.54 and 3.30 $Å^{-1}$ (Figure S2), corresponding with S−O and Fe···S pairs, respectively. This is again consistent with inner-sphere binuclear bidentate complexes reported in previous d-PDF[69] and EXAFS[61,69] studies. The Fe···S peak amplitude in the d-PDFs increased with decreasing the pH (Figure S2), which suggests an increase in the abundance of SO_4^{2-} inner-sphere complexes at pH 3.0 ± 0.2. At lower pHs, singly coordinated hydroxyls (Fe−OH) protonate and form weak Fe-OH_2^+ functional groups that can be easily displaced by SO_4^{2-} favoring the formation of inner-sphere complexes.[45]

Sulfate is known to form both inner- and outer-sphere surface complexes on Fh that vary with pH.[42,43,48,53,69−73] We used *in situ* ATR-FTIR experiments to examine this variation at pH conditions relevant to our experiments. The results showed the coexistence of inner- and outer-sphere SO_4^{2-} complexes. At pH 5.5 ± 0.2, the presence of SO_4^{2-} produced two peaks consistent with the intact asymmetric (1099 cm^{-1}) and symmetric (977 cm^{-1}) stretches of outer-sphere complexes (Figure S3a). Decreasing the pH to 3.0 ± 0.2 caused the peak at 1099 cm^{-1} to split into three peaks at 1170, 1111, and 1050 cm^{-1}, corresponding to SO_4^{2-} inner-sphere complexes, in agreement with previous IR studies.[53,69,72] Both outer- and inner-sphere complexes contribute to the absorbance feature at 977 cm^{-1}.[53] As shown, this feature increases with decreasing pH due to an increase in the fraction of inner-sphere complexes[45] (Figure S3). This is in agreement with our d-PDF results, as well as results from several other studies.[53,61,69] For example, Gu et al.[61] showed that decreasing pH from 5.5 to 3.0 caused the fraction of inner-sphere complexes to increase from 20 ± 5 to 80 ± 5% at pH and ionic strength (I = 0.1 M) conditions similar to our experiments.

Nitrate complexation on Fh was also studied using *in situ* ATR-FTIR. At pH 5.5 ± 0.2, the presence of NO_3^- produced a broad peak at 1365 cm^{-1} (Figure S3b), consistent with a previous study.[74] Due to similarities in symmetry, the spectra for hydrated outer-sphere surface complexes on Fh are similar to NO_3^- in solution.[45] Thus, we interpret the peak at 1365 cm^{-1} as corresponding with NO_3^- outer-sphere complexes. Decreasing pH resulted in the appearance of two smaller peaks at 1337 and 1385 cm^{-1}, which have been interpreted as corresponding with a minor proportion of NO_3^- inner-sphere complexes[69] that are not affected significantly by the pH range used in our experiments. This confirms the previous studies,[4,5,75] suggesting that NO_3^- predominantly forms outer-sphere complexes on Fh.

The different behavior of oxyanions during their complexation on Fh may be ascribed to their different ionic potential (IP = Z/r). Langmuir[76] proposed that smaller ions with higher charge make stronger inner-sphere bonds on the surface of solids. The ionic potential for NO_3^-, SO_4^{-2}, and AsO_4^- is 0.50, 0.87, and 1.21, respectively, mirroring the type and strength of their surface complexes from predominantly weak outer-sphere complexes for NO_3^-,[4,5,75] to a mixture of outer-sphere and inner-sphere complexes for SO_4^{2-},[42,43,48,53,70−73] and predominantly strong inner-sphere complexes for AsO_4^{3-}.[37,38,52,77,78] The oxyanions used in the present study were selected because their distinctive surface complexation behaviors make them useful for evaluating the effects of oxyanion surface complexation type and strength on the rate and pathway of Fh transformation.

All of the experiments were performed in an air-equilibrated solution containing DIC, which can compete with oxyanions for the available Fh surface sites and decrease the adsorption of oxyanions.[79,80] The percentage distribution of DIC species and their concentration was calculated using MINTEQ showing that HCO_3^- (16%) and H_2CO_3 (84%) were dominant DIC species for the chemical conditions used in this study. The

https://doi.org/10.1021/acs.est.2c04971
Environ. Sci. Technol. 2022, 56, 15672−15684

Table 1. Variation in the Concentration of Oxyanions at Each Stage of the Experiments

	initial concentration (mM)			amount adsorbed (mM)			amount on the surface at steady state (mM)					
							NO_3^-		SO_4^{2-}		AsO_4^{3-}	
sample	NO_3^-	SO_4^{2-}	AsO_4^{3-}	NO_3^-[a]	SO_4^{2-}	AsO_4^{3-}	buffered	nonbuffered	buffered	nonbuffered	buffered	nonbuffered
FhN	100			60.9 (0.3)[b]			54.9 (0.3)	55.1 (0.3)				
FhS	100	5.00			2.18 (0.02)				1.30 (0.02)	1.70 (0.02)		
FhAs	100		5.00			5.00					5.00	5.00

[a]The adsorption of NO_3^- is very low in the presence of SO_4^{2-} and AsO_4^{3-}, so it was not reported for FhS and FhAs. [b]The numbers in parentheses are standard errors.

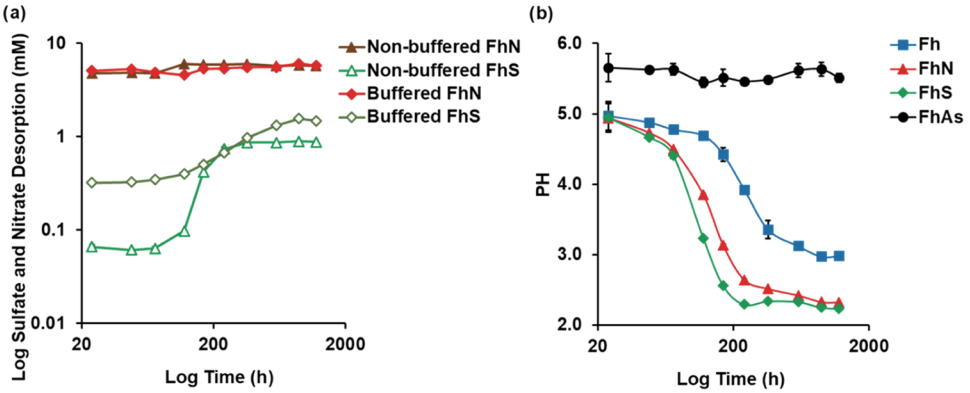

Figure 1. (a) Solution concentrations of NO_3^- and SO_4^{2-} with aging. The error bars corresponded to standard error (n = 3). (b) pH versus time for nonbuffered experiments with or without oxyanions present.

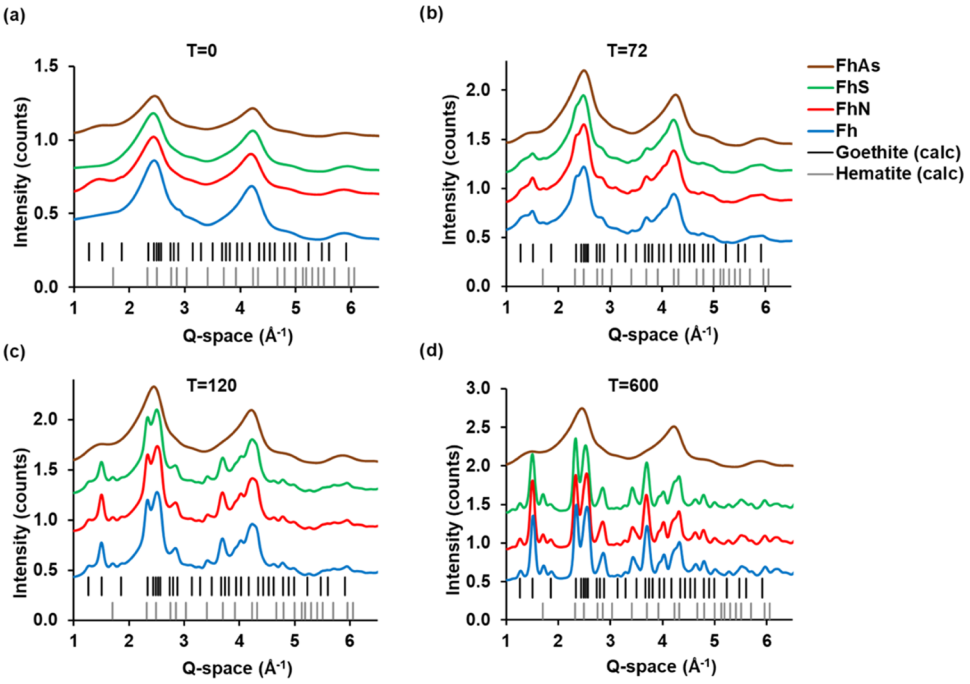

Figure 2. Synchrotron powder diffraction data for selected buffered samples at (a) 0 (i.e., prior to aging), (b) 72, (c) 120, and (d) 600 h of aging. These selected time points provide the best visualization of the transformation process; after 600 h of aging, the changes in the peaks become subtle and are similar to the peaks at 600 h.

overall concentration of DIC at pH 5.5 was ~0.016 mM (0.0003 DIC/Fh molar ratio), which is significantly lower than the concentration of oxyanions. In comparison, the oxyanion/Fh molar ratio was 1.9 for NO_3^- and 0.1 for both SO_4^{2-} and AsO_4^{3-}. A surface complexation modeling approach was used to investigate the contribution of DIC species to the adsorption process in the absence and presence of oxyanions. The results showed that adsorbed DIC occupied <0.05% of the Fh surface for the control Fh, and the presence of oxyanions would lower the amount of surface DIC even further. Thus, we conclude that the amount of DIC present in our experiments does not significantly impact the adsorption of oxyanions on Fh.

https://doi.org/10.1021/acs.est.2c04971
Environ. Sci. Technol. 2022, 56, 15672−15684

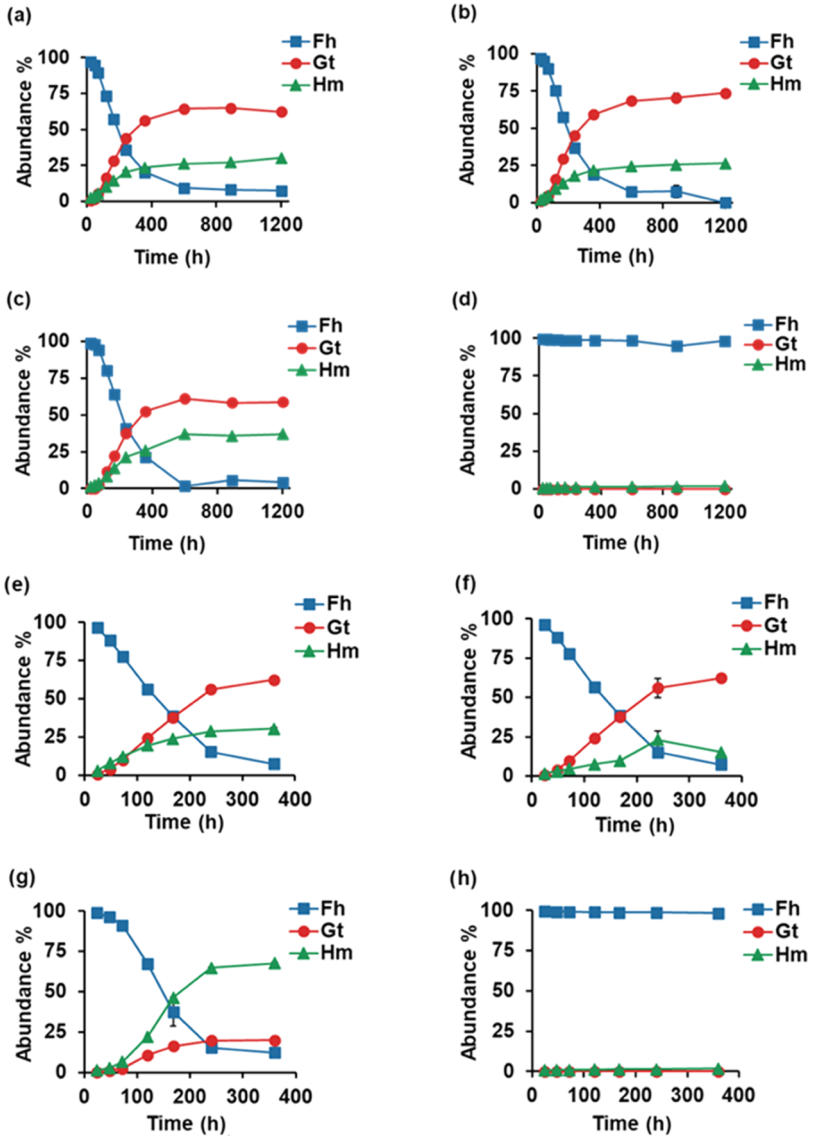

Figure 3. Abundances of Fh, Gt, and Hm with time for the buffered experiments. (a) Fh control, (b) NO_3^--adsorbed Fh, (c) SO_4^{2-}-adsorbed Fh, and (d) AsO_4^{3-}-adsorbed Fh; and the nonbuffered experiments (e) Fh control, (f) NO_3^--adsorbed Fh, (g) SO_4^{2-}-adsorbed Fh, and (h) AsO_4^{3-}-adsorbed Fh. Note that the total time shown is less in the nonbuffered experiments due to the faster rates of transformation. The error bars correspond to standard error (n = 3). Error bars for some samples in these and other figures are smaller than the symbol.

Oxyanion Sorption Behavior. The adsorption and desorption behaviors of NO_3^-, SO_4^{2-}, and AsO_4^{3-} were significantly different during the Fh aging experiments. The variation in the concentration of oxyanions at each stage of the experiments is shown in Table 1. Solution chemical analysis showed that 60.9 ± 0.3 mM NO_3^- (initial concentration 100 mM) were adsorbed to FhN during the batch adsorption experiment. With aging, ~5.8 mM NO_3^- was released to solution during aging with no significant differences observed between the buffered and nonbuffered experiments (Figure 1a). As described in the previous section, the behavior of NO_3^- was consistent with dominantly outer-sphere complexation on the surface of Fh. The initial SO_4^{2-} adsorption was less than half (2.18 ± 0.02 mM out of 5 mM) and the lowest of the different oxyanions. Sulfate also showed desorption with aging in both buffered and nonbuffered experiments (Figure 1a). Decreasing pH in the nonbuffered experiments resulted in an increase in the proportion of SO_4^{2-} inner-sphere complexes which slowed the desorption of SO_4^{2-} in the early stages of the nonbuffered experiment (Figure 1b). However, with progressive Fh transformation, more SO_4^{2-} was desorbed such that the overall amount of SO_4^{2-} desorption was higher (1.70 ± 0.02 mM) in the nonbuffered experiment. Finally, AsO_4^{3-} was completely adsorbed (5 out of 5 mM) on Fh at the beginning of the experiments, and no measurable desorption occurred in either the buffered or nonbuffered systems. This behavior is attributed to the strong AsO_4^{3-} inner-sphere complexation on Fh and limited transformation, as described in the next section.

Ferrihydrite Transformation Products. Synchrotron powder diffraction data were used to identify the crystalline products of Fh transformation. The intensity vs Q-space ($Q = \frac{4\pi \sin\theta}{\lambda}$) plots for selected time points from each sample series are shown in Figure 2. The broad peaks in the t = 0 h samples for all series were indicative of two-line Fh.[6] The aging

https://doi.org/10.1021/acs.est.2c04971
Environ. Sci. Technol. 2022, 56, 15672−15684

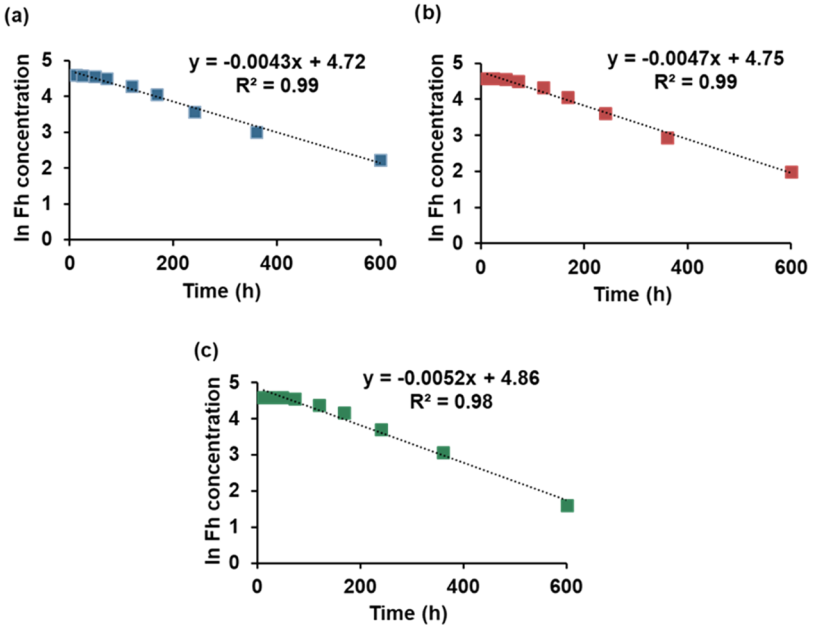

Figure 4. ln Fh concentration vs time for (a) control Fh, (b) FhN, and (c) FhS of the buffered experiment. The slope of the lines equals $-(k_{Gt} + k_{Ht})$.

of the control Fh, FhN, and FhS samples resulted in the development of relatively sharp and intense (Bragg) peaks during aging that can be indexed with the known structures of Gt and Hm, with no other crystalline phase present (Figure 2). In comparison, the diffraction data for the samples adsorbed with AsO_4^{3-} (FhAs) showed no obvious changes with aging (Figure 2). Figure S4 shows the corresponding PDFs for selected samples from each series.

Linear combination fitting of the real-space PDFs was used to quantify the abundances of the Fh and its transformation products during aging. Figure 3 shows the results of LCF analysis as the fraction of Fh, Gt, and Hm versus time for the buffered and nonbuffered experiments with or without oxyanions present. The buffered and nonbuffered samples showed similar overall trends during the transformation for the control Fh, but the nonbuffered experiments reached steady state earlier (Figure 3). The nonbuffered control Fh transformed almost entirely (93%) to Gt and Hm in <360 h. In comparison, the buffered control Fh took more than 600 h to reach the same extent of transformation (Figure 3). In the nonbuffered experiments, with the exception of FhAs, pH significantly decreased from an initial pH of 5.5 ± 0.2 to 3.36 ± 0.03 for the control Fh, 2.52 ± 0.01 for FhN, and 2.36 ± 0.02 for FhS at steady state (Figure 1b). The stronger decrease of pH for FhN and FhS compared to the control Fh suggests that the transformation of Fh and desorption of oxyanions both control the pH in the nonbuffered samples,[8] which led to the faster transformation of the nonbuffered experiment. Control experiments showed that in the absence of oxyanions, Fh aged at 70 ± 1.5 °C transformed to a mixture that is primarily Gt with a lesser amount of Hm. The amount of Gt that formed in the buffered samples was more than 2 times higher than Hm, resulting in significantly more Gt (64.4 ± 0.1%) than Hm (26.3 ± 0.1%) at steady state. The nonbuffered control showed similar amounts of Gt (62.2 ± 1.9%) and Hm (30.3 ± 1.0%) as the buffered samples. The reaction equations for the Fh transformation and oxyanion desorption that produces H^+ are provided in Text S2.

Nitrate and SO_4^{2-} had different effects on the amounts of Hm and Gt formed during Fh transformation. Weak outer-sphere NO_3^- adsorption increased Gt formation relative to Hm, with more Gt forming in both the buffered (73.6 ± 0.2%) and nonbuffered (71.9 ± 0.1%) experiments relative to the control (~64%). In comparison, the abundance of Hm was 24.2 ± 0.1 and 15.2 ± 0.1% for the buffered and nonbuffered FhNs, respectively, compared with ~ 26−30% for the control. In the case of SO_4^{2-}, which forms a mixture of inner- and outer-sphere complexes, the rate of Hm formation increased, resulting in more Hm in both the buffered (36.9 ± 0.8%) and nonbuffered (67.7 ± 0.5%) samples relative to the control (~26−30%). The abundance of Gt was 58.8 ± 1.6 and 20.0 ± 0.1% for the buffered and nonbuffered FhSs.

For the buffered samples, the Gt/(Hm + Gt) ratio did not significantly change for the control Fh (0.71 ± 0.03) and FhN (0.74 ± 0.03), but decreased to 0.62 ± 0.06 for FhS at steady state. This trend was more significant for the nonbuffered samples where the Gt/(Hm + Gt) ratio was 0.67 ± 0.08, 0.83 ± 0.04, and 0.23 ± 0.07 for control Fh, FhN, and FhS, respectively. Variation in the Gt/(Hm + Gt) ratio indicated that adsorbed NO_3^- induced Gt formation, whereas SO_4^{2-} promoted the formation of Hm.

The strong inner-sphere adsorption of AsO_4^{3-} significantly suppresses Fh transformation in the presence and absence of the buffer. The results show that <2% Hm was the only transformation product by the end of the aging experiments. The small amount of Fh transformation and suppression of AsO_4^{3-} desorption limit the release of H^+ to solution, which explains why pH is constant even in the nonbuffered FhAs during aging (Figure 1b).

Rate Model. Fh transformation reactions are controlled by the concentrations of Fh, H^+, and dissolved Fe. At pH 5.5 ± 0.2, the initial pH in this work, dissolved Fe produced from Fh dissolution, quickly precipitates as the product of trans-

https://doi.org/10.1021/acs.est.2c04971
Environ. Sci. Technol. 2022, 56, 15672−15684

Table 2. Pseudo-First-order Kinetic Parameters for the Buffered Ferrihydrite Transformation

sample	Gt_{eq} (%)[b]	Hm_{eq} (%)	slope[c] $-(k_{Gt} + k_{Hm})$	k_{Gt}/k_{Hm}[d]	k_{Gt} (h^{-1})[e]	k_{Hm} (h^{-1})
control Fh	64.36 (0.1)[a]	26.31 (0.1)	4.3×10^{-3} (6×10^{-5})	2.45 (4×10^{-3})	3.05×10^{-3} (7×10^{-5})	1.25×10^{-3} (2×10^{-5})
FhN	68.46 (0.1)	24.23 (0.1)	4.6×10^{-3} (6×10^{-5})	2.82 (0.02)	3.45×10^{-3} (6×10^{-5})	1.22×10^{-3} (2×10^{-5})
FhS	61.19 (0.1)	37.04 (0.7)	5.2×10^{-3} (9×10^{-5})	1.65 (0.04)	3.23×10^{-3} (1×10^{-4})	1.96×10^{-3} (6×10^{-5})

[a]Numbers in parentheses represent the standard error ($n = 3$). [b]The concentration of Hm and Gt at steady state (i.e., 600 h of aging). [c]The slope obtained from the $\ln[Fh]_t$ vs time plots in each respective experiment. [d]k_{Gt}/k_{Hm} was calculated using eq 2. [e]k_{Gt} and k_{Hm} calculated using eq 2 and the slopes of the lines that equals $-(k_{Gt} + k_{Hm})$.

formation (e.g., Gt). Thus, the dissolution of Fh that forms dissolved Fe controls the rate of transformation, but the precipitation of dissolved Fe does not limit the rate of reaction. In the nonbuffered experiment, the concentration of dissolved Fe at steady state was very low compared to the initial mass of Fh (5 g L^{-1}), ranging from 0.00115(1) g L^{-1} for Fh control (pH = 3.36 ± 0.03) to 0.00153(2) g L^{-1} for FhN (pH = 2.52 ± 0.0), and 0.0008(2) g L^{-1} for FhS (pH = 2.36 ± 0.02). This suggests that dissolved Fe was not a rate-limiting step even at more acidic pH. Dissolved Fe was not detected in the supernatant of all of the buffered experiments and the nonbuffered FhAs.

In the absence of buffer, the Fh transformation produces H^+, which decreases the pH of the system (Figure 1b). The addition of the MES buffer maintained the pH at 5.5 ± 0.2, fixing the H^+ concentration and rate of Fh dissolution. The MES buffer used in this work is expected to weakly interact with the Fh surfaces through electrostatic interaction.[81] We note that the MES buffer in our experiments was added after the oxyanions had already been introduced to the system and allowed to adsorb to Fh until steady state was reached. This was done to minimize competition between the buffer and the oxyanions for Fh surface sites. Detailed reaction pathways are illustrated in Text S2.

The Fh transformation in the buffered experiment follows the pseudo-first-order kinetic reaction

$$\ln[Fh]_t = \ln[Fh]_0 - (k_{Gt} + k_{Hm})t \quad (1)$$

where $[Fh]_t$ is the concentration of Fh at time t, $[Fh]_0$ is the initial concentration of Fh, and k_{Gt} and k_{Hm} are the rate constants for Gt and Hm formation, respectively. The plot of the natural logarithm of $[Fh]_t$ versus time is a straight line with a slope of $-(k_{Gt} + k_{Hm})$ (Figure 4).

Also, the following relationship was derived

$$\frac{k_{Gt}}{k_{Hm}} = \frac{[Gt_{eq}]}{[Hm_{eq}]} \quad (2)$$

where $[Gt_{eq}]$ and $[Hm_{eq}]$ are the abundance of Gt and Hm at steady state, respectively. Gt and Hm rate constants can be calculated using the slopes of the lines and eq 2 (Table 2). The acquired values can then be used in the following equations to calculate the rate of Gt and Hm formation.

$$\frac{d[Gt]}{dt} = k_{Gt}[Fh]_t \quad (3)$$

$$\frac{d[Hm]}{dt} = k_{Hm}[Fh]_t \quad (4)$$

The rate law derivations for both Fh transformation and Gt and Hm formation are provided in Text S3.

A pseudo-first-order kinetic model works well for modeling Fh transformation experiments at constant pH but is based on certain assumptions that are not applicable to nonbuffered systems. This model did yield a linear dependence for the $\ln[Fh]_t$ vs time plots for the data from our nonbuffered experiments (Figure S5), similar to the results reported by others for nonbuffered systems.[10,11] However, first-order kinetic reactions are based on the assumption that H^+ does not control the Fh transformation rate, whereas pH has been reported to be an important controlling factor for the Fh transformation.[8−12,17,19] The pH significantly decreased in all of the nonbuffered samples during the transformation of Fh, with the exception of FhAs (Figure 1b). A more complex rate model with a higher order is needed to describe the role of H^+ during Fh transformation. Thus, any kinetic model describing a nonbuffered Fh transformation should account for the variation of H^+ concentration. For this reason, the remaining discussion focuses mainly on the impacts of adsorbed oxyanions on the rate and pathway of Fh transformation in the buffered experiments.

Rate of Transformation. The derived rate equations were used to determine the rate of Fh transformation in each sample series. Figure 4 shows the plot of $\ln[Fh]_t$ vs time for the buffered samples (i.e., Fh control, FhN, FhS). A straight line was achieved for all of the sample series, confirming that the Fh concentration is the only rate-limiting step and that the dissolved Fe precipitates rapidly and does not control the rate of Fh transformation. This suggests that oxyanions released from the surface during the Fh transformation do not significantly stabilize the dissolved Fe, which may be due to the faster kinetic of the dissolved Fe precipitation than their complexation with the desorbed oxyanions. The R^2 for the first three points (up to 72 h) is >0.90, but still less than the R^2 obtained when fitting the data from the entire experiment. This may be due to an induction time needed for the formation of the first products of transformation and/or the effects caused by the presence of oxyanions on the Fh surfaces during the early stage of transformation. The values obtained from the plot of $\ln[Fh]_t$ vs time, and eqs 1−3 are shown in Table 2. FhS showed the highest slope ($5.2 \times 10^{-3} \pm 9 \times 10^{-5}$), although the values obtained for the Fh control and FhN were not significantly different. The k_{Gt}/k_{Hm} ratio was highest for the FhN series (2.82 ± 0.02). The FhN and FhS showed the highest rate constants for Gt ($3.45 \times 10^{-3} \pm 6 \times 10^{-5}$ h^{-1}) and Hm ($1.96 \times 10^{-3} \pm 6 \times 10^{-5}$ h^{-1}) formation, respectively.

The measured rate of Gt formation was higher than that of Hm in all experiments except in the presence of adsorbed AsO_4^{3-} (Figure 5). Overall, Gt formation was fastest in the case of adsorbed NO_3^- (FhN series) and slowest with adsorbed SO_4^{2-} (FhS). Goethite was not observed during the first 48 h in FhS, but its rate progressively increased beyond this initial period and then eventually (i.e., after 240 h) formed at a rate similar to that of the control Fh. The rate of Hm formation was similar to the control, and FhN samples during the entire transformation process. The SO_4^{2-} adsorbed samples displayed a higher rate of Hm formation, which was

https://doi.org/10.1021/acs.est.2c04971
Environ. Sci. Technol. 2022, 56, 15672−15684

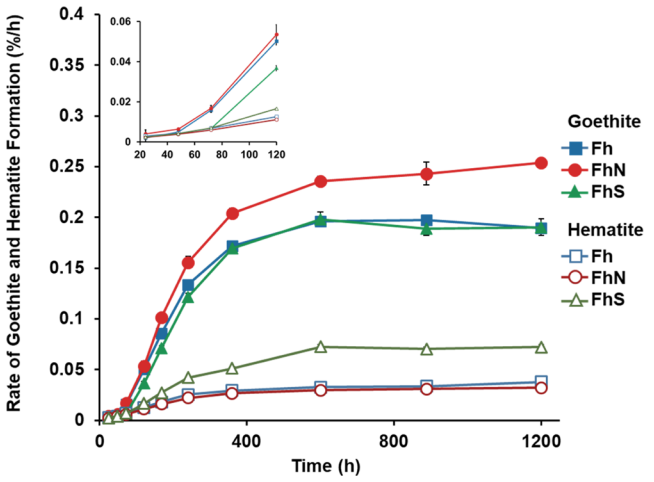

Figure 5. Rate of Gt and Hm formation for the buffered control Fh, FhN, and FhS samples. The error bars correspond to standard error (n = 3). The inset is shown for clarity of early time points.

almost twice that of the Fh control and FhN at the end of the experiment.

The rate of transformation was not quantified for the nonbuffered samples due to the complexity of the reactions that result from the large decrease in pH during aging. However, it is apparent that the transformation in the nonbuffered experiments reaches steady state much faster compared to the buffered samples. As shown in Figure 3, the nonbuffered samples reached steady state in 240−360 h of aging, whereas the buffered samples required >600 h to reach completion.

The rates of Gt or Hm formation for the control Fh were subtracted from the rates for FhN and FhS to further examine the impacts of NO_3^-or SO_4^{2-} in the buffered experiments, as well as to compare these changes with the measured concentrations of desorbed oxyanions with aging. As shown in Figure 6a, the corrected rate of Gt formation in the presence of NO_3^- increased beyond that of the control, starting at 120 h. In contrast, the rate of Hm formation in FhN was slightly lower than that of the control. The measured desorbed NO_3^- concentration was approximately constant and not strongly affected by the changing rates of Gt or Hm formation. The presence of SO_4^{2-} had the opposite effect as NO_3^- on the rates of Gt and Hm formation. The corrected rates showed that Gt formation was slower with SO_4^{2-} present until the transformation reached steady state at approximately 600 h (Figure 6b). The onset of Hm formation was delayed, but the rate increased beyond that of the control starting at 120 h, which tracks well with the increase in the solution concentration of dissolved SO_4^{2-}. Further, the low SO_4^{2-} concentrations for aging times <120 h suggest that adsorbed SO_4^{2-} slowed the rate of Gt formation compared to the control in the early stage of transformation.

Pathways of Fh Transformation and Effects of Oxyanions. The presence of NO_3^- favored the transformation of Fh to Gt relative to Hm compared with the control. The effect of NO_3^- on Gt formation is attributed to an increase in the degree of hydration at the Fh surface. At pH 5.5 ± 0.2, the hydration sphere of NO_3^-[82,83] may exchange with the Fh surface species, which include OH^0 and O^-, in addition to OH_2^+,[61] providing additional water for Fh dissolution and subsequent precipitation of Gt. This suggests that NO_3^- may

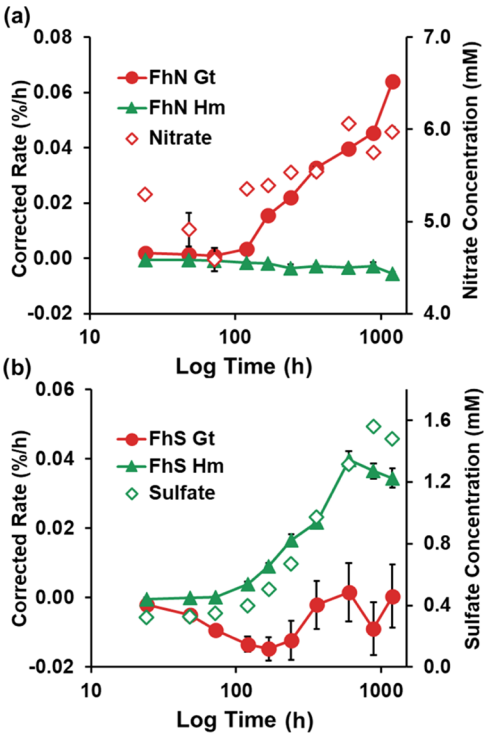

Figure 6. Measured rates of Gt and Hm formation for (a) FhN and (b) FhS in the buffered experiments corrected by subtracting the rates of the Fh control. Positive and negative values indicate rates of formation that are faster or slower relative to the control, respectively. Zero values approximately match the control rates. Desorbed NO_3^- or SO_4^{2-} concentrations vs time shown for comparison.

promote the dissolution/recrystallization pathway during Fh transformation. As demonstrated here, SO_4^{2-} also forms a significant proportion of outer-sphere complexes at pH 5.5 ± 0.2; however, its presence did not increase the rate of Gt formation, as is the case for NO_3^-.

Adsorbed SO_4^{2-} induced Hm formation during Fh transformation due to the presence and impact of SO_4^{2-} inner-sphere complexes. Ferrihydrite surfaces are positively charged at pH 5.5 ± 0.2 below the PZNPC of Fh (~8),[84,85] which increases the number of weak Fe-OH_2^+ functional groups[45] favoring ligand exchange[40,61] and an increase in the fraction of SO_4^{2-} inner-sphere (vs outer-sphere) complexes.[45,61] In the buffered experiment, SO_4^{2-} adsorbed Fh transformed to both Gt and Hm; however, the final fraction of Hm was approximately ~9% more than the control. Hematite formation (67.7 ± 0.5%) was favored relative to Gt (20.0 ± 0.1%) even more during aging in the nonbuffered FhS, which we would expect to exhibit a higher proportion of SO_4^{2-} inner-sphere complexes. We attribute this effect to the removal of the SO_4^{2-} hydration sphere prior to its inner-sphere adsorption on the Fh surface.[61] Inner-sphere complexes are expected to dehydrate the Fh surfaces, which may result in decreasing the dissolution of Fh, suppressing the formation of Gt, and promoting transformation to less hydrated products. In addition, the removal of the hydration sphere facilitates the direct binding of SO_4^{2-} on the surface, which leads to the consumption of positive surface charges and a decrease in the electrostatic repulsion between Fh particles,[68,86] thus, promoting aggregation of particles during the Fh transformation.[59] Based on the Derjaguin, Landau, Verwey, and Overbeek (DLVO) theory, decreasing surface protonation induces faster

https://doi.org/10.1021/acs.est.2c04971
Environ. Sci. Technol. 2022, 56, 15672−15684

particle aggregation.[57−59,87] The positive correlation of inner-sphere complexation, surface dehydration, the relatively high fraction of Hm, and Gt suppression suggests that Hm is primarily formed through dehydration/aggregation of Fh nanoparticles. This agrees with the results recently reported by Zhu et al.,[88] who showed that inner-sphere adsorbed oxalate promotes Hm nucleation during Fh transformation. They suggested that oxalate complexes change the Hm formation mechanism from ion-by-ion growth to near-interface nucleation and attachment.

Arsenate adsorption dramatically slowed the rate of Fh transformation and exclusively formed Hm, although the transformation was far from complete. Because AsO_4^{3-} forms primarily strong inner-sphere complexes with Fh,[37,38] it has higher strength than SO_4^{2-} to dehydrate the Fh surface,[61] suppress the dissolution/precipitation pathway, consume positive surface charges, and promote the transformation to Hm. Although the relative surface dehydration favors the formation of Hm (as opposed to Gt), the strong inner-sphere attachment and limited surface hydration appear to inhibit Fh transformation.[21] Ligands such as AsO_4^{3-} are generally expected to stabilize Fe(III) on the Fh surface, thereby inhibiting dissolution,[27] which explains the slow overall rate of transformation relative to the control. In addition to stabilizing, strongly adsorbed AsO_4^{3-} may inhibit OA processes by populating the interfaces between adjoining Fh particles.[89] The prolonged induction time for the formation of Hm in the FhAs samples indicates that nucleation is involved, which requires at least some degree of hydration within the aggregates.[21]

Inner-sphere SO_4^{2-} surface complexes did not inhibit the Fh transformation as in the case of AsO_4^{3-}. We attribute this to the relatively small fraction of the inner-sphere SO_4^{2-} at pH 5.5 ± 0.2. The lower rate of Gt formation in FhS compared with the control might also be related to the presence of inner-sphere complexes that partially limit surface hydration and stabilize the surface with respect to dissolution. The rate was slowest from 72 to 120 h, which ultimately resulted in a lower final fraction of Gt relative to the control. The rate of Hm formation in the presence of SO_4^{2-} began to accelerate relative to the control at 120 h and reached a maximum rate at 240 h. Overall, the transformation of Fh to Hm was promoted by the presence of SO_4^{2-}, which we attribute to the presence of inner-sphere complexes that partly dehydrate the surface and consume positive surface charges.[61] As described previously, outer-sphere NO_3^- complexes promote Gt formation by providing additional water for dissolving Fh. However, the results indicated that outer-sphere SO_4^{2-} did not promote Gt formation at pH 5.5 ± 0.2 when inner-sphere SO_4^{2-} complexes were also present.

Prior studies have reached different conclusions regarding the primary mechanism of Fh transformation to Gt. Some have suggested the importance of dissolution/recrystallization;[9,22,23] however, more recent experiments using high-resolution transmission electron microscopy (TEM) indicated that Gt may form primarily via aggregation by OA.[12,57,59,90,91] The discrepancies may be explained by differences in experimental conditions and characterization methods. Differentiating these two mechanisms is not possible using bulk characterization methods (e.g., powder diffraction) alone, as direct imaging is required to understand aggregation behavior and detect the presence of OA. On the other hand, using TEM for imaging the phase transformation of poorly crystalline 2-line Fh was also reported to be challenging.[17] Similarly, differences in the type of Fh (i.e., 2-line vs 6-line) used in transformation experiments may also have an effect on the mechanism. For example, previous work has shown that the rate of Fh particle dissolution increases with decreasing size.[90] They suggested that Oswald ripening controls the behavior of small Fh particles even when the oriented aggregation is the dominant pathway. This may be important as numerous prior studies of Fh transformation to Gt have used 6-line Fh.[12,57,59,90,91] The 2-line Fh used as the starting material in the present study will be less stable and dissolve more readily, particularly at elevated temperatures,[59,90] which should favor dissolution/recrystallization. Our results suggest that outer-sphere NO_3^- complexes promote Gt formation by increasing the degree of hydration at the Fh surface, which enhances even more dissolution. Yet, our data do not rule out Gt formation by aggregation and OA; therefore, this pathway may also control the Gt formation to a certain extent. Moreover, Gt nuclei formed through dissolution/recrystallization[27] may later grow to larger particles via aggregation by OA.[12,91] In addition, the adsorption of the oxyanions released from Fh may impact the morphology of the transformation products and their growth via OA. Future experiments and additional characterization, for example, by cryogenic TEM, are needed to better understand the impacts of adsorbed oxyanions on OA.

In summary, the type and strength of oxyanion surface complexes on Fh strongly influenced the rate and pathway of transformation to Gt or Hm. The degree of hydration at the mineral-water interface plays a major role in both pathways, as dissolution/recrystallization requires water to dissolve the metastable Fh particles, and dehydration is necessary to promote aggregation by OA of Fh. Oxyanion can control the degree of hydration on the Fh surface. Nitrate forms predominantly weak outer-sphere adsorption complexes that increase the rate of Gt formation, which we attribute to an increase in the degree of hydration at the Fh surface due to exchange with the hydration sphere for NO_3^-. This enhances Fh dissolution and formation of the dissolved Fe that precipitates as ferric hydroxide (Gt; FeO(OH)). In contrast, Hm formation increases in the presence of inner-sphere complexes (AsO_4^{3-}) or a mixture of inner- and outer-sphere complexes (SO_4^{2-}). Strong inner-sphere complexes e.g., AsO_4^{3-} dramatically slow Fh transformation by inhibiting dissolution resulting in the minor transformation to Hm and no evidence of Gt. Inner-sphere complexation of oxyanions is expected to displace water, dehydrate the Fh surface, and consume positive surface charges that induces the aggregation of particles as Hm. Thus, we attribute the correlation between increasing Hm formation rate to dehydration resulting from the occurrence of inner-sphere complexes. Further studies are needed to better understand how different types and strengths of oxyanion surface complexes modify the degree of hydration on the Fh surface.

IMPLICATIONS

This work demonstrates the impact of oxyanion surface complexation type and strength on the rate and pathway of Fh transformation. We showed that outer-sphere oxyanion complexes promote the formation of Gt, whereas Hm formation is favored for inner-sphere complexes. Also, our

https://doi.org/10.1021/acs.est.2c04971
Environ. Sci. Technol. 2022, 56, 15672−15684

kinetic model showed that oxyanion surface complexes decrease the rate of Fh transformation such that almost no transformation occurred in the presence of strong AsO_4^{3-} inner-sphere complexes. We propose that the degree of surface hydration is a critical factor controlling the rate and pathway of Fh transformation. Oxyanion adsorption acts as a kinetics barrier by changing the degree of hydration through either providing (e.g., NO_3^-) or removing (e.g., AsO_4^{3-}) water from the Fh surface. With increasing strength and proportion of oxyanion inner-sphere complexes, more water is removed from the Fh surface, promoting the formation of Hm, and decreasing the rate of transformation. We suggest that the type and strength of oxyanion complexes govern the rate and pathway of Fh transformation, not the species themselves. This was evidenced by the distinct impact of adsorbed SO_4^{2-} on the rate and pathway of Fh transformation. With decreasing pH, the inner-sphere SO_4^{2-} complexes increase, resulting in a significant increase in the amount of Hm compared to pH 5.5 ± 0.2 where the SO_4^{2-} outer-sphere complexes are dominant. Also, our results showed that the Fh transformation could release weakly adsorbed oxyanions (i.e., NO_3^- and SO_4^{2-}) to solution, which has implications for the transport and fate of adsorbed surface species. This work introduces a new analytical approach and kinetic model that allows a direct quantification of the products of Fh transformation and describes their rate and pathway.

■ ASSOCIATED CONTENT

Supporting Information

The Supporting Information is available free of charge at https://pubs.acs.org/doi/10.1021/acs.est.2c04971.

Surface complexation model (Text S1); ferrihydrite transformation reaction (Text S2); rate law derivation (Text S3); surface complexation reactions, equilibrium constants, and plane charge distribution (Table S1); d-PDF of arsenate adsorption on ferrihydrite obtained by subtraction of a nitrate-adsorbed ferrihydrite from an arsenate-adsorbed ferrihydrite made in a background of nitrate, the two major peaks at 1.71 and 3.29 $Å^{-1}$ correspond to As−O and As−Fe (Figure S1); d-PDF of sulfate adsorption on ferrihydrite obtained by subtraction of a nitrate-adsorbed ferrihydrite from a sulfate-adsorbed ferrihydrite made in a background of nitrate, the two major peaks at 1.54 and 3.3 $Å^{-1}$ correspond to As−O and As−Fe (Figure S2); ART-FTIR spectra of sulfate and nitrate adsorbed on ferrihydrite (Figure S3); PDFs for samples at 0 (fresh sample before aging), 240, 360, and 600 h of aging (Figure S4); ln Fh concentration vs time for control Fh, FhN, and FhS of the nonbuffered experiment (Figure S5) (PDF)

■ AUTHOR INFORMATION

Corresponding Author

Alireza Namayandeh − *Department of Geosciences, Virginia Tech, Blacksburg, Virginia 24061, United States;* orcid.org/0000-0003-2942-3245; Email: anamayandeh@vt.edu

Authors

Olaf J. Borkiewicz − *Advanced Photon Source, Argonne National Laboratory, Lemont, Illinois 60439, United States*

Nefeli M. Bompoti − *Department of Civil and Environmental Engineering, University of Connecticut, Storrs, Connecticut 06269, United States;* orcid.org/0000-0003-2799-188X

Maria Chrysochoou − *Department of Civil and Environmental Engineering, University of Connecticut, Storrs, Connecticut 06269, United States*

F. Marc Michel − *Department of Geosciences, Virginia Tech, Blacksburg, Virginia 24061, United States; Virginia Tech, Division of Nanoscience, Academy of Integrated Science, Blacksburg, Virginia 24061, United States*

Complete contact information is available at: https://pubs.acs.org/10.1021/acs.est.2c04971

Notes

The authors declare no competing financial interest.

■ ACKNOWLEDGMENTS

F.M.M. gratefully acknowledges financial support provided by the National Science Foundation through CAREER-1652237 and the Virginia Tech National Center for Earth and Environmental Nanotechnology Infrastructure ("NanoEarth", NSF Cooperative Agreement 1542100). This research used resources of the Advanced Photon Source, a U.S. Department of Energy (DOE) Office of Science User Facility operated for the DOE Office of Science by Argonne National Laboratory under Contract No. DE-AC02-06CH11357.

■ REFERENCES

(1) Fendorf, S.; Eick, M. J.; Grossl, P.; Sparks, D. L. Arsenate and chromate retention mechanisms on goethite. 1. Surface structure. *Environ. Sci. Technol.* **1997**, *31*, 315.

(2) Hiemstra, T.; Antelo, J.; Rahnemaie, R.; Riemsdijk, W. H. V. Nanoparticles in natural systems I: The effective reactive surface area of the natural oxide fraction in field samples. *Geochim. Cosmochim. Acta* **2010**, *74*, 41−58.

(3) Sparks, D. L.*Environmental Soil Chemistry*, 2nd ed.; Academic: San Diego, California: London, 2003.

(4) Sparks, D. L.Fundamentals of Soil Chemistry. In *Encyclopedia of Water: Science, Technology, and Society*; Wiley, 2019; pp 1−11.

(5) Sposito, G.*The Chemistry of Soils*, 2nd ed.; Oxford University Press: Oxford, 2008.

(6) Michel, F. M.; Ehm, L.; Antao, S. M.; Lee, P. L.; Chupas, P. J.; Liu, G.; Strongin, D. R.; Schoonen, M. A. A.; Phillips, B. L.; Parise, J. B. The Structure of Ferrihydrite, a Nanocrystalline Material. *Science* **2007**, *316*, 1726.

(7) Michel, F. M.; Barrón, V.; Torrent, J.; Morales, M. P.; Serna, C. J.; Boily, J. F.; Liu, Q.; Ambrosini, A.; Cismasu, A. C.; Brown, G. E. Ordered ferrimagnetic form of ferrihydrite reveals links among structure, composition, and magnetism. *Proc. Natl. Acad. Sci. U.S.A.* **2010**, *107*, 2787.

(8) Cudennec, Y.; Lecerf, A. The transformation of ferrihydrite into goethite or hematite, revisited. *J. Solid State Chem.* **2006**, *179*, 716−722.

(9) Schwertmann, U.; Stanjek, H.; Becher, H. H. Long-term in vitro transformation of 2-line ferrihydrite to goethite/hematite at 4, 10, 15 and 25 °C. *Clay Miner.* **2004**, *39*, 433−438.

(10) Das, S.; Hendry, M. J.; Essilfie-Dughan, J. Transformation of two-line ferrihydrite to goethite and hematite as a function of pH and temperature. *Environ. Sci. Technol.* **2011**, *45*, 268−275.

(11) Das, S.; Hendry, M. J.; Essilfie-Dughan, J. Effects of adsorbed arsenate on the rate of transformation of 2-line ferrihydrite at pH 10. *Environ. Sci. Technol.* **2011**, *45*, 5557−5563.

(12) Burleson, D. J.; Penn, R. L. Two-step growth of goethite from ferrihydrite. *Langmuir* **2006**, *22*, 402−409.

(13) Hu, S.; Lu, Y.; Peng, L.; Wang, P.; Zhu, M.; Dohnalkova, A. C.; Chen, H.; Lin, Z.; Dang, Z.; Shi, Z. Coupled kinetics of ferrihydrite

transformation and As (V) sequestration under the effect of humic acids: a mechanistic and quantitative study. *Environ. Sci. Technol.* **2018**, *52*, 11632−11641.
(14) Lu, Y.; Hu, S.; Wang, Z.; Ding, Y.; Lu, G.; Lin, Z.; Dang, Z.; Shi, Z. Ferrihydrite transformation under the impact of humic acid and Pb: kinetics, nanoscale mechanisms, and implications for C and Pb dynamics. *Environ. Sci.: Nano* **2019**, *6*, 747−762.
(15) Schwertmann, U.; Friedl, J.; Stanjek, H. From Fe (III) ions to ferrihydrite and then to hematite. *J. Colloid Interface Sci.* **1999**, *209*, 215−223.
(16) Shimizu, M.; Zhou, J.; Schröder, C.; Obst, M.; Kappler, A.; Borch, T. Dissimilatory reduction and transformation of ferrihydrite-humic acid coprecipitates. *Environ. Sci. Technol.* **2013**, *47*, 13375−13384.
(17) Soltis, J. A.; Feinberg, J. M.; Gilbert, B.; Penn, R. L. Phase Transformation and Particle-Mediated Growth in the Formation of Hematite from 2-Line Ferrihydrite. *Cryst. Growth Des.* **2016**, *16*, 922−932.
(18) Zhang, D.; Wang, S.; Wang, Y.; Gomez, M. A.; Duan, Y.; Jia, Y. The transformation of two-line ferrihydrite into crystalline products: effect of pH and media (sulfate versus nitrate). *ACS Earth Space Chem.* **2018**, *2*, 577−587.
(19) Schwertmann, U.; Murad, E. J. C.; Minerals, C. Effect of pH on the formation of goethite and hematite from ferrihydrite. *Clays Clay Miner.* **1983**, *31*, 277−284.
(20) Das, S.; Essilfie-Dughan, J.; Hendry, M. J. J. C. G. Fate of adsorbed arsenate during phase transformation of ferrihydrite in the presence of gypsum and alkaline conditions. *Chem. Geol.* **2015**, *411*, 69−80.
(21) Schwertmann, U.; Cornell, R. M.*Iron Oxides in the Laboratory: Preparation and Characterization*, 2nd ed.; Wiley-VCH: Weinheim, 2000.
(22) Schwertmann, U. B.; Cornell, R. M.*Iron Oxides in the Laboratory Preparation and Characterization*; Wiley-VCH: Weinheim, 2000. http://sfx.ethz.ch/sfx_locater?sid=ALEPH:EBI01&genre=book&isbn=9783527296699.
(23) Mackay, A. In *Some Aspects of the Topochemistry of the Iron Oxides and Hydroxides, Reactivity of Solids*, Proceedings of the Fourth International Symposium on the Reactivity of Solids, 1960; pp 571−583.
(24) De Yoreo, J. J.; Gilbert, P. U. P. A.; Sommerdijk, N. A. J. M.; Penn, R. L.; Whitelam, S.; Joester, D.; Zhang, H.; Rimer, J. D.; Navrotsky, A.; Banfield, J. F.; Wallace, A. F.; Michel, F. M.; Meldrum, F. C.; Cölfen, H.; Dove, P. M. Crystallization by particle attachment in synthetic, biogenic, and geologic environments. *Science* **2015**, *349*, No. aaa6760.
(25) Penn, R. L.; Oskam, G.; Strathmann, T. J.; Searson, P. C.; Stone, A. T.; Veblen, D. R. Epitaxial assembly in aged colloids. *J. Phys. Chem. B* **2001**, *105*, 2177−2182.
(26) Banfield, J. F.; Welch, S. A.; Zhang, H.; Ebert, T. T.; Penn, R. L. Aggregation-based crystal growth and microstructure development in natural iron oxyhydroxide biomineralization products. *Science* **2000**, *289*, 751−754.
(27) Bilardello, D.; Banerjee, S. K.; Volk, M. W. R.; Soltis, J. A.; Penn, R. L. Simulation of Natural Iron Oxide Alteration in Soil: Conversion of Synthetic Ferrihydrite to Hematite Without Artificial Dopants, Observed With Magnetic Methods. *Geochem., Geophys., Geosyst.* **2020**, *21*, No. e2020GC009037.
(28) Jiang, Z.; Liu, Q.; Dekkers, M. J.; Barrón, V.; Torrent, J.; Roberts, A. P. J. Control of Earth-like magnetic fields on the transformation of ferrihydrite to hematite and goethite. *Sci. Rep.* **2016**, *6*, No. 30395.
(29) Jentzsch, T. L.; Penn, R. L. Influence of aluminum doping on ferrihydrite nanoparticle reactivity. *J. Phys. Chem. B* **2006**, *110*, 11746.
(30) Hu, Y.; Li, Q.; Lee, B.; Jun, Y. Aluminum affects heterogeneous Fe (III) (Hydr) oxide nucleation, growth, and Ostwald ripening. *Environ. Sci. Technol.* **2014**, *48*, 299.
(31) Sheng, A.; Liu, J.; Li, X.; Qafoku, O.; Collins, R. N.; Jones, A. M.; Pearce, C. I.; Wang, C.; Ni, J.; Lu, A.; Rosso, K. M. Labile Fe(III) from sorbed Fe(II) oxidation is the key intermediate in Fe(II)-catalyzed ferrihydrite transformation. *Geochim. Cosmochim. Acta* **2020**, *272*, 105−120.
(32) Hansel, C. M.; Benner, S. G.; Fendorf, S. Competing Fe(II)-Induced Mineralization Pathways of Ferrihydrite. *Environ. Sci. Technol.* **2005**, *39*, 7147−7153.
(33) Voelz, J. L.; Arnold, W. A.; Penn, R. L. Redox-induced nucleation and growth of goethite on synthetic hematite nanoparticles. *Am. Mineral.* **2018**, *103*, 1021−1029.
(34) Aeppli, M.; Kaegi, R.; Kretzschmar, R.; Voegelin, A.; Hofstetter, T. B.; Sander, M. J. Electrochemical analysis of changes in iron oxide reducibility during abiotic ferrihydrite transformation into goethite and magnetite. *Environ. Sci. Technol.* **2019**, *53*, 3568−3578.
(35) ThomasArrigo, L. K.; Kaegi, R.; Kretzschmar, R. Ferrihydrite Growth and Transformation in the Presence of Ferrous Iron and Model Organic Ligands. *Environ. Sci. Technol.* **2019**, *53*, 13636−13647.
(36) Jones, A. M.; Collins, R. N.; Rose, J.; Waite, T. D. The effect of silica and natural organic matter on the Fe(II)-catalysed transformation and reactivity of Fe(III) minerals. *Geochim. Cosmochim. Acta* **2009**, *73*, 4409−4422.
(37) Antelo, J.; Arce, F.; Fiol, S. Arsenate and phosphate adsorption on ferrihydrite nanoparticles. Synergetic interaction with calcium ions. *Chem. Geol.* **2015**, *410*, 53−62.
(38) Harrington, R.; Hausner, D. B.; Bhandari, N.; Strongin, D. R.; Chapman, K. W.; Chupas, P. J.; Middlemiss, D. S.; Grey, C. P.; Parise, J. B. Investigation of Surface Structures by Powder Diffraction: A Differential Pair Distribution Function Study on Arsenate Sorption on Ferrihydrite. *Inorg. Chem.* **2010**, *49*, 325−330.
(39) Kubicki, J. D.; Paul, K. W.; Kabalan, L.; Zhu, Q.; Mrozik, M. K.; Aryanpour, M.; Pierre-Louis, A. M.; Strongin, D. R. ATR-FTIR and Density Functional Theory Study of the Structures, Energetics, and Vibrational Spectra of Phosphate Adsorbed onto Goethite. *Langmuir* **2012**, *28*, 14573.
(40) Namayandeh, A.; Kabengi, N. Calorimetric study of the influence of aluminum substitution in ferrihydrite on sulfate adsorption and reversibility. *J. Colloid Interface Sci.* **2019**, *540*, 20−29.
(41) Hug, S. J. In Situ Fourier transform infrared measurements of sulfate adsorption on hematite in aqueous solutions. *J. Colloid Interface Sci.* **1997**, *188*, 415.
(42) Fukushi, K.; Aoyama, K.; Yang, C.; Kitadai, N.; Nakashima, S. Surface complexation modeling for sulfate adsorption on ferrihydrite consistent with in situ infrared spectroscopic observations. *Appl. Geochem.* **2013**, *36*, 92.
(43) Fukushi, K.; Sverjensky, D. A. A surface complexation model for sulfate and selenate on iron oxides consistent with spectroscopic and theoretical molecular evidence. *Geochim. Cosmochim. Acta* **2007**, *71*, 1.
(44) Manceau, A.; Charlet, L. The Mechanism of Selenate Adsorption on Goethite and Hydrous Ferric Oxide. *J. Colloid Interface Sci.* **1994**, *168*, 87−93.
(45) Peak, D.; Ford, R. G.; Sparks, D. L. An in situ ATR-FTIR investigation of sulfate bonding mechanisms on goethite. *J. Colloid Interface Sci.* **1999**, *218*, 289.
(46) Tian, L.; Shi, Z.; Lu, Y.; Dohnalkova, A. C.; Lin, Z.; Dang, Z. Kinetics of Cation and Oxyanion Adsorption and Desorption on Ferrihydrite: Roles of Ferrihydrite Binding Sites and a Unified Model. *Environ. Sci. Technol.* **2017**, *51*, 10605−10614.
(47) Wang, X.; Gu, C.; Feng, X.; Zhu, M. Sulfate local coordination environment in schwertmannite. *Environ. Sci. Technol.* **2015**, *49*, 10440.
(48) Wang, X.; Wang, Z.; Peak, D.; Tang, Y.; Feng, X.; Zhu, M. Quantification of Coexisting Inner- and Outer-Sphere Complexation of Sulfate on Hematite Surfaces. *ACS Earth Space Chem.* **2018**, *2*, 387−398.
(49) Arai, Y.; Sparks, D. L. ATR-FTIR Spectroscopic Investigation on Phosphate Adsorption Mechanisms at the Ferrihydrite−Water Interface. *J. Colloid Interface Sci.* **2001**, *241*, 317−326.

(50) Elzinga, E. J.; Kretzschmar, R. In situ ATR-FTIR spectroscopic analysis of the co-adsorption of orthophosphate and Cd(II) onto hematite. *Geochim. Cosmochim. Acta* **2013**, *117*, 53−64.
(51) Hinkle, M. A. G.; Wang, Z.; Giammar, D. E.; Catalano, J. G. Interaction of Fe(II) with phosphate and sulfate on iron oxide surfaces. *Geochim. Cosmochim. Acta* **2015**, *158*, 130.
(52) Jain, A.; Loeppert, R. H. Effect of Competing Anions on the Adsorption of Arsenate and Arsenite by Ferrihydrite. *J. Environ. Qual.* **2000**, *29*, 1422−1430.
(53) Johnston, C. P.; Chrysochoou, M. Mechanisms of Chromate, Selenate, and Sulfate Adsorption on Al-Substituted Ferrihydrite: Implications for Ferrihydrite Surface Structure and Reactivity. *Environ. Sci. Technol.* **2016**, *50*, 3589−3596.
(54) Johnston, C. P.; Chrysochoou, M. Mechanisms of chromate adsorption on hematite. *Geochim. Cosmochim. Acta* **2014**, *138*, 146.
(55) Kubicki, J. D.; Kabengi, N.; Chrysochoou, M.; Bompoti, N. Density functional theory modeling of chromate adsorption onto ferrihydrite nanoparticles. *Geochem. Trans.* **2018**, *19*, 8.
(56) Fischer, W.; Schwertmann, U. J. The formation of hematite from amorphous ir on (iii) hydroxide. *Clays Clay Miner.* **1974**, *23*, 33−37.
(57) Penn, R. L.; Tanaka, K.; Erbs, J. J. Size dependent kinetics of oriented aggregation. *J. Cryst. Growth* **2007**, *309*, 97−102.
(58) Burrows, N. D.; Hale, C. R. H.; Penn, R. L. Effect of Ionic Strength on the Kinetics of Crystal Growth by Oriented Aggregation. *Cryst. Growth Des.* **2012**, *12*, 4787−4797.
(59) Burrows, N. D.; Hale, C. R. H.; Penn, R. L. Effect of pH on the Kinetics of Crystal Growth by Oriented Aggregation. *Cryst. Growth Des.* **2013**, *13*, 3396−3403.
(60) Liao, S.; Wang, X.; Yin, H.; Post, J. E.; Yan, Y.; Tan, W.; Huang, Q.; Liu, F.; Feng, X. Effects of Al substitution on local structure and morphology of lepidocrocite and its phosphate adsorption kinetics. *Geochim. Cosmochim. Acta* **2020**, *276*, 109−121.
(61) Gu, C.; Wang, Z.; Kubicki, J. D.; Wang, X.; Zhu, M. X-ray Absorption Spectroscopic Quantification and Speciation Modeling of Sulfate Adsorption on Ferrihydrite Surfaces. *Environ. Sci. Technol.* **2016**, *50*, 8067−8076.
(62) Yang, X.; Juhas, P.; Farrow, C. L.; Billinge, S. J.xPDFsuite: An End-to-End Software Solution for High Throughput Pair Distribution Function Transformation, Visualization and Analysis. 2014, arXiv:1402.3163. arXiv.org e-Print archive. https://arxiv.org/abs/1402.3163.
(63) Ressler, T. WinXAS: a Program for X-ray Absorption Spectroscopy Data Analysis under MS-Windows. *J. Synchrotron Radiat.* **1998**, *5*, 118−122.
(64) Carabante, I.; Grahn, M.; Holmgren, A.; Kumpiene, J.; Hedlund, J. Adsorption of As (V) on iron oxide nanoparticle films studied by in situ ATR-FTIR spectroscopy. *Colloids Surf., A* **2009**, *346*, 106−113.
(65) Waychunas, G. A.; Rea, B. A.; Fuller, C. C.; Davis, J. A. Surface chemistry of ferrihydrite: Part 1. EXAFS studies of the geometry of coprecipitated and adsorbed arsenate. *Geochim. Cosmochim. Acta* **1993**, *57*, 2251−2269.
(66) Sherman, D. M.; Randall, S. R. Surface complexation of arsenic(V) to iron(III) (hydr)oxides: structural mechanism from ab initio molecular geometries and EXAFS spectroscopy. *Geochim. Cosmochim. Acta* **2003**, *67*, 4223−4230.
(67) Antelo, J.; Avena, M.; Fiol, S.; López, R.; Arce, F. J. Effects of pH and ionic strength on the adsorption of phosphate and arsenate at the goethite−water interface. *J. Colloid Interface Sci.* **2005**, *285*, 476−486.
(68) Antelo, J.; Fiol, S.; Pérez, C.; Mariño, S.; Arce, F.; Gondar, D.; López, R. Analysis of phosphate adsorption onto ferrihydrite using the CD-MUSIC model. *J. Colloid Interface Sci.* **2010**, *347*, 112−119.
(69) Zhu, M.; Northrup, P.; Shi, C.; Billinge, S. J.; Sparks, D. L.; Waychunas, G. A. Structure of sulfate adsorption complexes on ferrihydrite. *Environ. Sci. Technol. Lett.* **2014**, *1*, 97.
(70) Fukushi, K.; Aoyama, K.; Yang, C.; Kitadai, N.; Nakashima, S. Surface complexation modeling for sulfate adsorption on ferrihydrite consistent with in-situ infrared spectroscopic observations. *Appl. Geochem.* **2013**, *36*, 92.
(71) Parfitt, R. L.; Smart, R. S. C. The mechanism of sulfate adsorption on iron oxides. *Soil Sci. Soc. Am. J.* **1978**, *42*, 48.
(72) Peak, D.; Elzinga, E.; Sparks, D.; Selim, H.Understanding Sulfate Adsorption Mechanisms on Iron(III) Oxides and Hydroxides: Results from ATR-FTIR Spectroscopy. In *Heavy Metals Release in Soils*; Lewis Publishers Inc: Boca Raton, 2001; p 167.
(73) Zhu, M.; Northrup, P.; Shi, C.; Billinge, S. J.; Sparks, D. L.; Waychunas, G. A. Structure of sulfate adsorption complexes on ferrihydrite. *Environ. Sci. Technol. Lett.* **2014**, *1*, 97.
(74) Gan, F.; Wu, K.; Ma, F.; Du, C. In Situ Determination of Nitrate in Water Using Fourier Transform Mid-Infrared Attenuated Total Reflectance Spectroscopy Coupled with Deconvolution Algorithm. *Molecules* **2020**, *25*, No. 5838.
(75) Harvey, O. R.; Rhue, R. D. Kinetics and energetics of phosphate sorption in a multi-component Al(III)−Fe(III) hydr-(oxide) sorbent system. *J. Colloid Interface Sci.* **2008**, *322*, 384−393.
(76) Langmuir, D.*Aqueous Environmental*; Prentice Hall, 1997.
(77) Adra, A.; Morin, G.; Ona-Nguema, G.; Brest, J. Arsenate and arsenite adsorption onto Al-containing ferrihydrites. Implications for arsenic immobilization after neutralization of acid mine drainage. *Appl. Geochem.* **2016**, *64*, 2.
(78) Arai, Y.; Elzinga, E. J.; Sparks, D. L. X-ray absorption spectroscopic investigation of arsenite and arsenate adsorption at the aluminum oxide−water interface. *J. Colloid Interface Sci.* **2001**, *235*, 80.
(79) Appelo, C. A. J.; Van Der Weiden, M. J. J.; Tournassat, C.; Charlet, L. Surface Complexation of Ferrous Iron and Carbonate on Ferrihydrite and the Mobilization of Arsenic. *Environ. Sci. Technol.* **2002**, *36*, 3096−3103.
(80) Zachara, J. M.; Ainsworth, C. C.; Cowan, C. E.; Thomas, B. L. Sorption of binary mixtures of aromatic nitrogen heterocyclic compounds on subsurface materials. *Environ. Sci. Technol.* **1987**, *21*, 397−402.
(81) Hiemstra, T.; Mendez, J. C.; Li, J. Evolution of the reactive surface area of ferrihydrite: time, pH, and temperature dependency of growth by Ostwald ripening. *Environ. Sci.: Nano* **2019**, *6*, 820−833.
(82) Fournier, J. A.; Carpenter, W.; De Marco, L.; Tokmakoff, A. Interplay of Ion−Water and Water−Water Interactions within the Hydration Shells of Nitrate and Carbonate Directly Probed with 2D IR Spectroscopy. *J. Am. Chem. Soc.* **2016**, *138*, 9634−9645.
(83) Loganathan, P.; Vigneswaran, S.; Kandasamy, J. Enhanced removal of nitrate from water using surface modification of adsorbents—A review. *J. Environ. Manage.* **2013**, *131*, 363−374.
(84) Geelhoed, J. S.; Hiemstra, T.; Van Riemsdijk, W. H. Phosphate and sulfate adsorption on goethite: Single anion and competitive adsorption. *Geochim. Cosmochim. Acta* **1997**, *61*, 2389−2396.
(85) Cismasu, A. C.; Levard, C.; Michel, F. M.; Brown, G. E., Jr Properties of impurity-bearing ferrihydrite II: Insights into the surface structure and composition of pure, Al- and Si-bearing ferrihydrite from Zn(II) sorption experiments and Zn K-edge X-ray absorption spectroscopy. *Geochim. Cosmochim. Acta* **2013**, *119*, 46−60.
(86) Hiemstra, T.; Zhao, W. Reactivity of ferrihydrite and ferritin in relation to surface structure, size, and nanoparticle formation studied for phosphate and arsenate. *Environ. Sci.: Nano* **2016**, *3*, 1265−1279.
(87) Derjaguin, B. V.; Landau, L. D. Theory of the stability of strongly charged lyophobic sols and of the adhesion of strongly charged particles in solutions of electrolytes. *Acta Physicochim. URSS* **1941**, *14*, 633−662.
(88) Zhu, G.; Sushko, M. L.; Loring, J. S.; Legg, B. A.; Song, M.; Soltis, J. A.; Huang, X.; Rosso, K. M.; De Yoreo, J. J. J. N. Self-similar mesocrystals form via interface-driven nucleation and assembly. *Nature* **2021**, *590*, 416−422.
(89) Yuwono, V. M.; Burrows, N. D.; Soltis, J. A.; Do, T. A.; Penn, R. L. J. F. D. Aggregation of ferrihydrite nanoparticles in aqueous systems. *Faraday Discuss.* **2012**, *159*, 235−245.

(90) Li, D.; Nielsen, M. H.; Lee, J. R. I.; Frandsen, C.; Banfield, J. F.; De Yoreo, J. J. Direction-Specific Interactions Control Crystal Growth by Oriented Attachment. *Science* **2012**, *336*, 1014−1018.
(91) Yuwono, V. M.; Burrows, N. D.; Soltis, J. A.; Penn, R. L. J. J. Oriented aggregation: formation and transformation of mesocrystal intermediates revealed. *J. Am. Chem. Soc.* **2010**, *132*, 2163−2165.

https://doi.org/10.1021/acs.est.2c04971
Environ. Sci. Technol. 2022, 56, 15672−15684